

See discussions, stats, and author profiles for this publication at: <https://www.researchgate.net/publication/11710015>

Characterization of Fe Plaque and Associated Metals on the Roots of Mine-Waste Impacted Aquatic Plants

ARTICLE *in* ENVIRONMENTAL SCIENCE AND TECHNOLOGY · NOVEMBER 2001

Impact Factor: 5.33 · DOI: 10.1021/es0105459 · Source: PubMed

CITATIONS

181

READS

120

4 AUTHORS, INCLUDING:



Colleen Hansel

Woods Hole Oceanographic Institution

70 PUBLICATIONS 2,455 CITATIONS

SEE PROFILE



Scott Fendorf

Stanford University

270 PUBLICATIONS 10,839 CITATIONS

SEE PROFILE



Matthew Newville

University of Chicago

278 PUBLICATIONS 11,965 CITATIONS

SEE PROFILE

Characterization of Fe Plaque and Associated Metals on the Roots of Mine-Waste Impacted Aquatic Plants

COLLEEN M. HANSEL AND
SCOTT FENDORF*

Department of Geological and Environmental Sciences,
Stanford University, Stanford, California 94305

STEVE SUTTON AND MATT NEWVILLE

Consortium for Advanced Radiation Sources and
Department of Geophysical Sciences, University of Chicago,
Chicago, Illinois 60637

Iron plaque on aquatic plant roots are ubiquitous and sequester metals in wetland soils; however, the mechanisms of metal sequestration are unresolved. Thus, characterizing the Fe plaque and associated metals will aid in understanding and predicting metal cycling in wetland ecosystems. Accordingly, microscopic and spectroscopic techniques were utilized to identify the spatial distributions, associations, and chemical environments of Fe, Mn, Pb, and Zn on the roots of a common, indigenous wetland plant (*Phalaris arundinacea*). Iron forms a continuous precipitate on the root surface, which is composed dominantly of ferrihydrite (ca. 63%) with lesser amounts of goethite (32%) and minor levels of siderite (5%). Although Pb is juxtaposed with Fe on the root surface, it is complexed to organic functional groups, consistent with those of bacterial biofilms. In contrast, Mn and Zn exist as discrete, isolated mixed-metal carbonate (rhodochrosite/hydrozincite) nodules on the root surface. Accordingly, the soil–root interface appears to be a complex biochemical environment, containing both reduced and oxidized mineral species, as well as bacterial-induced organic–metal complexes. As such, hydrated iron oxides, bacterial biofilms, and metal carbonates will influence the availability and mobility of metals within the rhizosphere of aquatic plants.

Introduction

The partitioning and specific binding mechanisms of metals within the soil, water, and plants have important implications for delineating potential bioavailability and/or release of metals upon changing physicochemical conditions within aquatic environments. An understanding of metal complexation within the rhizosphere of aquatic plants is of ecological and nutritional importance inasmuch as the chemical form of metals affects their mobility. Observations of elevated metal concentrations within root relative to shoot tissue suggest that wetland plants adopt either external or internal exclusion mechanisms to hinder translocation of metals to the aerial tissue (1). For instance, in saturated soils, radial oxygen diffusion and subsequent iron plaque formation on plant

roots has been suggested as a potential mechanism for waterlogging tolerance (2). Specifically, a physiological adaptation of aquatic plants allows for the absorption of $O_{2(g)}$ in aerial tissue followed by translocation and release of oxygen into the rhizosphere (3, 4). Iron oxidizes rapidly in the presence of molecular $O_{2(g)}$ (5) resulting in Fe (hydr)oxide plaque precipitation on the root epidermis. Iron-oxidizing bacteria may also play a substantial role in Fe plaque development on plant roots (6, 7). Iron plaque on wetland and rice plant roots are suspected to limit the mobility of metals; however, the iron species and the mechanisms of contaminant immobilization are unresolved.

Iron plaque formation on roots is well-documented for a number of aquatic plant species, including *Oryza sativa*, *Typha latifolia*, *Phragmites australis*, *Juncus bulbosus*, *Aster tripolium*, and *Spartina alterniflora* (2, 4, 8–10). Iron plaque accumulation can account for up to 10% root dry weight and extend as much as 15–17 μm into the rhizosphere (11, 12). While a number of studies designate the plaque as consisting of iron hydroxides, the structural arrangement of the iron hydroxide has ranged from lepidocrocite to goethite to an “amorphous-like” hydroxide (11, 13–16). Furthermore, a recent study has proposed that the plaque consists of reduced (ferrous) iron and may therefore be composed of iron carbonate (siderite) (17). Due to large variation in the reactivity of the aforementioned Fe phases, this discrepancy in the mineralogical framework of the iron plaque makes assessment of its reactivity and subsequent role in metal sequestration difficult.

A number of metal(loid)s have been found associated with Fe plaque deposits, including Mn, Zn, Cu, and As (10, 16, 18). While correlations were evident between Fe and the aforementioned metals, the mechanisms of metal sequestration were not ascertained. Yet, knowledge of the speciation and structural environment of metals is imperative for predicting and modeling their fate and transport in anaerobic soils. Accordingly, the mineralogical framework of Fe plaque and the structural environment of associated metals on the roots of *Phalaris arundinacea*, a common, indigenous aquatic plant, were investigated. The spatial distribution and speciation of metal ions at the soil–root interface were examined using X-ray microprobe, X-ray fluorescence microtomography, X-ray absorption spectroscopy (XAS), and Raman spectroscopy.

Materials and Methods

Site Description. The Coeur d’Alene (CdA) mining district is located in the Idaho panhandle and has the largest recorded Ag production in the world as well as abundant quantities of Au, Cd, Cu, Pb, Sn, and Zn (19). The primary economic minerals are galena (PbS), sphalerite (ZnS), and Ag-bearing tetrahedrite ($\text{Cu}_{12}\text{Sb}_4\text{S}_{13}$). The gangue minerals within the region are chiefly quartz (SiO_2), sericite [fine-grained muscovite, $\text{KAl}_2(\text{AlSi}_3\text{O}_{10}(\text{OH})_2)$], ferroan dolomite [$\text{Ca}(\text{Mg}, \text{Fe}^{2+})(\text{CO}_3)_2$], and siderite (FeCO_3), but the region also hosts an abundance of calcite (CaCO_3), pyrite (FeS_2), chalcocopyrite (CuFeS_2), and pyrrhotite (Fe_{1-x}S , $x = 0\text{--}0.2$) (19, 20). Minor gangue minerals also include the carbonates, dolomite [$\text{CaMg}(\text{CO}_3)_2$], and ankerite [$\text{Ca}(\text{Mg}, \text{Fe}^{2+}, \text{Mn})(\text{CO}_3)_2$].

From nearly a century of mining in the CdA district, an estimated 115 million metric tons of mine tailings were produced with about 60% of them discharged directly into the South Fork of the CdA river (CdAR) (21). The Cataldo Mission Flats constitute the flood plain of the Main Stem of the CdAR and are located approximately 30 km southeast of the city of Coeur d’Alene and 50 km east of Lake Coeur d’Alene

* Corresponding author phone: (650)723-5238; fax: (650)725-2199; e-mail: fendorf@stanford.edu.

(22). Fluvially deposited and dredged mine tailings from the Main Stem of the CdAR are situated upon the flood plain (23), and consequently the flats contain elevated concentrations of As, Fe, Mn, Pb, and Zn (24, 25). Flooding of the CdAR results in wetlands within the contaminated flood plain, one of which is the focus of this study and is hereinafter referred to as the Cataldo wetland (25).

The Cataldo wetland water depths vary from 0 (summer) to 90 cm (winter), while corresponding soil temperatures fluctuate from 25 to 5 °C. The bulk wetland soil pH is circumneutral with values decreasing slightly with depth. Similarly, Eh values indicate a decreasing soil redox potential with depth and the presence of reducing conditions.

Experimental Sampling. Soil, water, and *Phalaris arundinacea* (reed canary-grass) samples were obtained from the Cataldo wetland. *Phalaris arundinacea* stands to account for ca. 20% of the vegetation inhabiting this site. *Phalaris arundinacea* is an emergent, perennial grass common to submerged areas where water levels fluctuate (e.g., wetlands). Plant samples were extracted from the wetland and transported on ice to the laboratory. Plants were then divided into root and shoot portions and washed thoroughly with double deionized water to remove residual soil. Plant roots were scrubbed lightly and observed optically to ensure residual soil removal. Concentrations of metals within the plant portions were determined using a wet digestion procedure consisting of nitric acid followed by successive additions of 30% hydrogen peroxide and heating. Soil cores were obtained using a 4 cm diameter PVC piston coring device (26). Soil samples underwent total digestions using a combination of acid additions, shaking, and heating (27). Water samples were collected using membrane separated diffusion cells (peepers) (26), and water samples were acidified with HCl. Supernatants were analyzed via inductively coupled plasma-optical emission spectroscopy (Thermo Jarrell Ash IRIS ICP-OES; Franklin, MA) with a 5% accuracy range, and quality control was checked every 15 samples. Detection limits were defined as 3σ (where σ is the standard deviation) of five blanks (28). Detection limits were as follows: Fe 0.01 mg L⁻¹, Mn 0.01 mg L⁻¹, Pb 0.02 mg L⁻¹, and Zn 0.02 mg L⁻¹.

Metal Spatial Distributions and Associations. Elemental distributions and associations for Fe, Mn, Pb, and Zn were determined using X-ray microprobe and X-ray fluorescence microtomography. Microtomography scans were performed at beamline (undulator) 13-ID-C at the Advanced Photon Source, Argonne National Laboratory. Roots were preserved by freeze-drying and stored in a dehydrator. The intact (unaltered) root was mounted on the rotation axis of a x-y-theta stepping motor stage. Fluorescence data were collected with a solid-state energy-dispersive X-ray detector which allows multiple elements to be detected simultaneously. The microtomography data were obtained by translating the root through the X-ray beam and collecting fluorescence at each 5 micron step. At each position, the fluorescence signal from a given element is proportional to the integrated number of atoms of that element along the ray transected by the beam. The sample is then rotated 0.5° about the vertical axis and the line scan repeated. The process is continued until the root has been rotated through a total of 180°, resulting in 2D “sinograms” for each element. After reconstruction by backprojection, these element-specific sinograms yield images of the element distributions within the internal cross-section of the root.

X-ray microprobe scans of Mn and Zn were performed on beamline 10.3.2 at the Advanced Light Source, Lawrence Berkeley National Laboratory. The scan covers a 250 × 250 μm section of the root with data collection at 5 μm increments.

Solid-Phase Structural Analysis of Root Precipitates. Iron, Mn, Pb, and Zn speciation and structural environments

were obtained via X-ray absorption spectroscopy (XAS). The XAS analyses were conducted on beamline 4-1 and 4-3 (8 pole wiggler) at the Stanford Synchrotron Radiation Laboratory (SSRL), running under dedicated conditions. The ring operated at 3 GeV with a current ranging from ≈100 mA to ≈50 mA. Energy selection was accomplished using either a Si(111) or Si(220) monochromator with an unfocused beam. The XAS data were recorded by fluorescent X-ray production using a wide-angle ionization chamber for all samples (29). A 3 μm filter (Z-1) for each element and Soller slits were used to minimize the effects of scattered primary radiation. Incident and transmitted intensities were measured with inline ionization chambers. Higher-order harmonic frequencies were rejected by detuning from the maximum incident intensity. X-ray absorption near edge structure (XANES) spectra were recorded over the energy range of -200 to +500 eV about the K-edge of iron (7111 eV). EXAFS spectra were collected from -200 to +1000 eV about the K-edge of Mn (6539 eV), Zn (9659 eV), and the L_{III}-edge of Pb (13 055 eV). Each scan was calibrated internally by placing a metal foil between the second and third inline ionization chambers and calibrating off the first inflection point of Fe⁰ (7111 eV), Mn⁰ (6539 eV), Zn⁰ (9659 eV), and Pb⁰ (13 055 eV). Between 7 and 12 individual spectra were averaged for each sample.

Iron XANES spectra were analyzed using the computer code WinXAS (30) and compared to standard spectra for mineralogical estimation. Averaged XANES spectra of model compounds and samples were background subtracted using a low-order polynomial function and normalized by setting the total atomic cross-sectional absorption to unity. The first derivative of each spectrum was obtained using a Savitzky-Golay algorithm. Manganese, Pb, and Zn spectra were analyzed using EXAFSPAK (EXAFS) software (31) by usual procedures (for example see ref 32). Conventional shell-by-shell fitting was conducted using the OPT module of EXAFSPAK. Variables in these fits include coordination number (N), interatomic distance (R), and a Debye-Waller disorder factor (σ^2) for each shell. Due to first-shell intensities, resulting in robust, unambiguous fits, and the unique metal-oxygen distances for rhodochrosite and hydrozincite, we restricted our analyses to these short distances for Mn and Zn. A set of reference standards for Fe and Pb were utilized to perform linear combination XANES and k³-weighted EXAFS spectra fitting, respectively. Linear fitting routines were used to reconstruct the unknown in order to determine the relative percentages of mineral phases within the samples. Linear combinations of empirical model spectra were optimized, where the only adjustable parameters were the fractions of each model compound contributing to the fit. Fits were optimized by minimizing the residual of the fit, defined as the normalized root square difference between the data and the fit.

Model Fe compounds used in spectroscopic analysis include iron sulfide (FeS), siderite (FeCO₃), ferrihydrite (Fe₂O₃·nH₂O), goethite (α-FeOOH), lepidocrocite (γ-FeOOH), hematite (α-Fe₂O₃), green rust (Fe^{II}_{6-*x*}Fe^{III}_{*x*}(OH)₁₂[(SO₄)_{*x*/2}·3H₂O]), and magnetite (Fe₃O₄). Siderite and magnetite were natural samples obtained from the Stanford University Mineral Collection. Goethite, ferrihydrite, and lepidocrocite were synthesized following the procedures of Schwertmann and Cornell (33) and green rust following Schwertmann and Fechter (34). Synthesized standards were verified using X-ray diffraction analysis (XRD). A modified data set of ca. 35 Pb L_{III}-EXAFS reference spectra were used in experimental spectra fitting (see ref 35). Modifications to the set include Pb adsorbed to biofilm of *Burkholderia cepacia* (a gram-negative rod), and a number of organic substrates including Pb adsorbed to glucuronate, polygalacturonate, oxalate, citrate, acetate, and glycerol-2-phosphate. Similarly, Pb sorbed to a biofilm-like substrate was constructed by reaction

TABLE 1. Metal Concentrations within the Soil, Solution, and Plants^a

	mg kg ⁻¹			
	Fe	Mn	Pb	Zn
soil	46 000	1600	1600	1300
plant roots	59 000	500	1200	950
plant shoots	1200	450	62	130
solution	0.23	0.06	BDL ^b	BDL ^b

^a Values expressed as means ($n = 3$); all relative standard deviations < 15%. ^b Below detection limit.

of Pb within the cell-biofilm matrix of *Burkholderia cepacia*. This standard accounts for the general class of functional groups associated with bacteria surfaces and exopolysaccharide matrix. Lead sorbed to goethite was used as a representative of the general class of Pb sorbed to Fe (hydr)oxides. The validity of this correlation is supported by previous investigations that reveal similar structures for Pb on hematite and hydrous ferric oxide (HFO) (36, 37).

Raman spectroscopy was also employed to verify XANES results and to identify the mineralogical component of the root plaque. Raman spectra were collected using a Kaiser Hololab Raman microscope equipped with a 785 nm diode laser and a charge-coupled device detector having 4 cm⁻¹ resolution. The laser was operated at 1 mW average power at the sample to reduce sample degradation caused by laser heating. The laser was focused through a 100X objective in order to maximize signal intensity. A minimum collection time for all samples was 30 s per spectrum, and at least 30 spectra were averaged over a Raman shift of 100–3500 cm⁻¹.

Results and Discussion

Metal Partitioning and Concentrations. Soil, water, and plant (*P. arundinacea*) samples were collected from the Cataldo wetland to determine total concentrations of Fe, Mn, Pb, and Zn. Metals are predominantly partitioned within the soil and plant roots, with solution concentrations being minimal (Table 1). Metal concentrations are substantially elevated in plant tissue, including both roots and shoots. The observed shoot and root metal concentrations are consistent with previous investigations of wetland plants in metal contaminated soils (38–40). Additionally, metal concentrations (excluding Mn) in the plant roots are severalfold higher than in shoots. Mass balance calculations of the metals in the wetland subsurface indicate that *P. arundinacea* roots are sequestering substantial concentrations of metals within the soil environment, accounting for greater than 12% Fe, 8% Mn, 4% Pb, and 5% Zn within the bulk soil (for more details see refs 25 and 41).

Speciation and Spatial Association of Fe and Pb. Elemental distributions and associations for Fe and Pb were resolved by obtaining a cross-sectional image (a slice) from the interior of intact roots through the epidermis and plaque using X-ray fluorescence microtomography (Figure 1). Iron and Pb are concentrated on the exterior of the root forming a surficial rind on the epidermis and have similar distribution patterns. X-ray absorption near-edge structure (XANES) spectra of the plaque reveals a predominance of Fe(III) in an oxo or hydroxyl coordination environment (Figure 2). The main-edge peak in the first derivative for *P. arundinacea* corresponds to that of ferric iron (7124 eV). On the basis of optimized fits using a linear combination of model compounds, the Fe plaque of *P. arundinacea* consists of approximately 63% ferrihydrite, 32% goethite, and 5% siderite (Figure 2). At the Fe concentrations of these materials, detection limits for specific phases are better than 5%. Thus, while the inclusion of siderite improves optimization, its level

approaches our limits of detection. Raman analyses supports the XANES findings that the root plaques contain a preponderance of short-range order hydrated iron oxides. Initial Raman spectra revealed diffuse peaks indicative of short-range order minerals, and following dehydration distinct peaks were obtained analogous to those for hematite (α -Fe₂O₃) (see Supporting Information).

The large surface area of hydrated iron oxides (which is often in excess of 200 m² g⁻¹) provides a reactive substrate for contaminant sequestration (e.g., Cd, As). Moreover, Pb has a specific and high affinity for iron (hydr)oxides (36, 42). Iron plaque, therefore, provides a reactive substrate for the attenuation of Pb and other metals. Consistent with the expected affinity of Pb for Fe (hydr)oxides, microtomography scans illustrate juxtapositioning of Fe and Pb (Figure 1); however, EXAFS spectroscopy reveals a more complex situation. The Pb–O interatomic distance of 2.4 Å does not correspond to published values (~2.27 Å) for Pb adsorption to Fe(III) (hydr)oxides (Figure 3a) (36, 37). Instead, the Pb–O distance is indicative of Pb complexes on an organic substrate, consistent with Pb adsorbed on humic acids ($R_{av} = 2.4$ Å) (43) and mineral-supported biofilms (44). Optimized fitting of the second shell EXAFS function was obtained with carbon (or similarly, N) as the backscattering atom at a distance of 3.4 Å, which is longer than the published range for humic substances (43). However, the structural complexity of organic substances cannot be fully accounted for in standard preparation. Previously, EXAFS spectra of Pb has been found to exhibit a distinct shape which reflects the nearest-neighbor coordination geometry (45). As such, comparison of EXAFS spectra to reference spectra for use in fingerprinting the structural environment of Pb in complex natural samples has been found useful in identifying Pb species (35, 45). Linear combinations of Pb EXAFS spectra from the Fe plaque are best represented by Pb adsorbed to a biofilm-like substrate and not Pb adsorbed on Fe(III) (hydr)oxides or to organic acids (Figure 3b). Although there appears to be residual features not mimicked by the standard spectra, the primary oscillations are well predicted with the Pb-biofilm adsorption spectra.

Although Pb does not appear to be complexed directly on Fe (hydr)oxides, microtomography images illustrate an intimate association between Fe and Pb on the root surface. Recently, the rhizosphere of aquatic plants has been recognized as an advantageous niche for diverse microbial communities, including methane- and Fe-oxidizing bacteria (6, 7, 46, 47). Substantial numbers of cells (up to 2×10^6 cells/mm²) have been found embedded in the iron oxide matrix on the roots of wetland plants (6). Additionally, a recent study of aquatic environments revealed that natural iron hydroxides were systematically found associated with humic material and extracellular polymeric substances (EPS), which mostly remained attached to the bacteria from which they were produced (48). Accordingly, the surfaces of aquatic plants are most likely coated by an iron hydroxide-biofilm-like matrix forming a continuous surficial rind around the root. Preferential adsorption of Pb onto either the Fe hydroxide, bacteria surfaces, or EPS will depend largely on Pb concentration and pH (44).

Speciation and Spatial Association of Mn and Zn. Microtomography and X-ray microprobe images illustrate a dissimilar distribution pattern for Mn and Zn relative to Fe and Pb, thus suggesting an alternative mechanism for precipitation/sorption at the soil–root interface (Figure 1). On the root surface, the concentrations of Mn and Zn are elevated in discrete zones on the exterior of the epidermis, whereas, in contrast, concentrations diminish in areas adjacent to these zones. Zinc and Mn are strongly correlated aside from the root interior where Mn concentrations are considerably higher. Additionally, Ca levels are elevated at

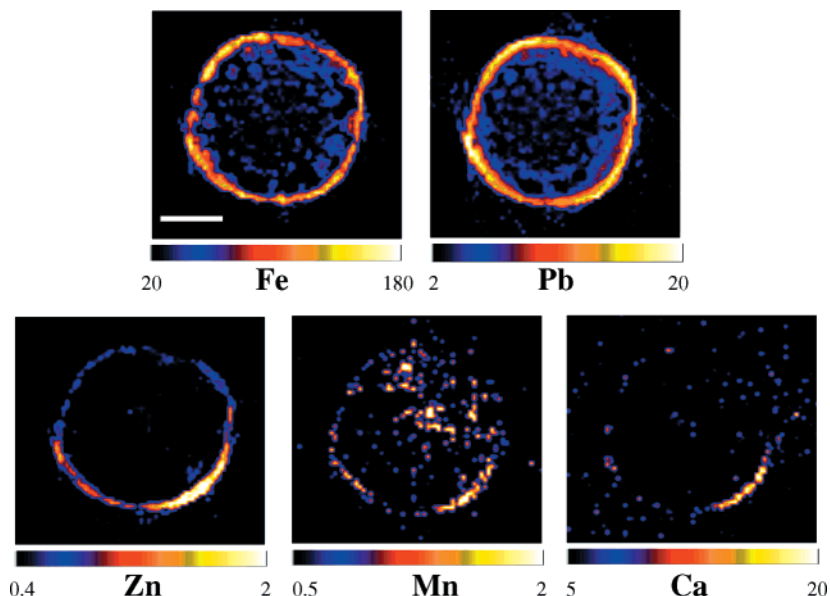


FIGURE 1. Metal distributions on and within roots of *Phalaris arundinacea* as depicted by fluorescence microtomography. The spatial distribution of Fe, Pb, Zn, Mn, and Ca within a cross-sectional slice of the grass root is illustrated. Scale bar represents 150 μm and color bars units are femtograms/ μm^3 .

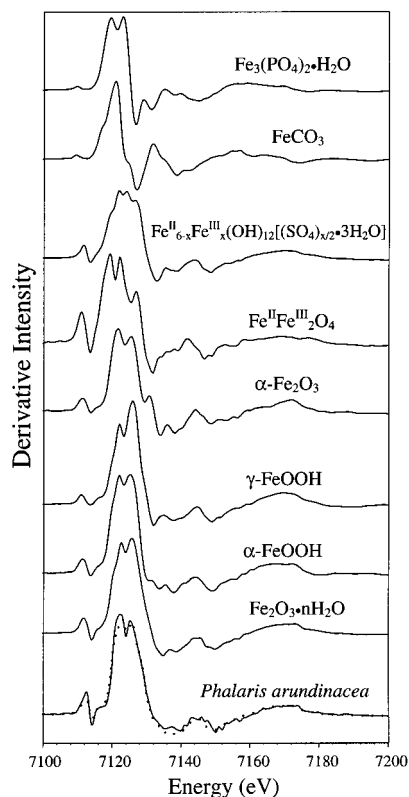


FIGURE 2. Iron first-derivative XANES spectra of model compounds and Fe plaque of *P. arundinacea*. The dotted line on the Fe plaque spectra represents the linear combination fitting of the spectra.

sites of Zn and Mn deposition on the root surface (Figure 1). A two-dimensional depiction of Mn and Zn distributions focused on the epidermis region further illustrates the strong correlation between Mn and Zn (Figure 4). Moreover, a nodular morphology of the Mn/Zn co- or mixed-precipitates is portrayed. Scans were performed on extensive portions of various roots, and the results were consistent with those illustrated in Figures 1 and 4.

The local coordination environment of Mn and Zn, determined using EXAFS spectroscopy (Figure 5), reveals that

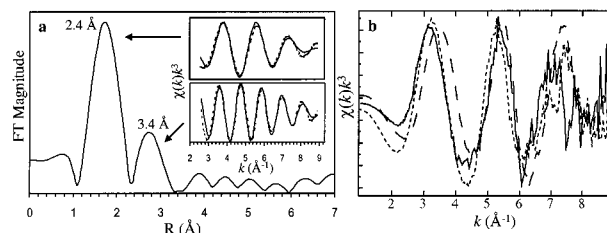


FIGURE 3. (a) Fourier transformed (FT) spectra of Pb on the root surface resulting in a radial structure function in real space (\AA). Fourier transform is not phase-shift corrected, and thus peak positions are less than true interatomic distances. Insets are the EXAFS spectra of the first shell (Pb–O) and second shell (Pb–C). Solid lines are the experimental spectra and dotted lines represent the theoretical fits. (b) Pb L_{III} -EXAFS spectra of root surface. Fit linear combination of model spectra for Pb adsorbed to biofilm (dotted) and Pb adsorbed to goethite (dashed) are overlain.

Mn is octahedrally coordinated by oxygen. The Mn–O interatomic distance is 2.20 \AA , which is in close agreement with published values (2.19 \AA) for rhodochrosite (MnCO_3) (49, 50). The first shell for Zn is a composite of three distinct sites (two octahedral and one tetrahedral) having an average of four different interatomic distances (2.08, 2.06, 2.15, and 1.96 \AA). The Zn–O(H) distances correspond to published values for hydrozincite [$\text{Zn}_5(\text{OH})_6(\text{CO}_3)_2$] (51, 52). Furthermore, root and bacterial respiration produces carbonate concentrations at the root surface approaching 5 mmol L^{-1} , thus allowing for enhanced carbonate precipitation even in mildly acidic pH environments (53). Accordingly, on the basis of the EXAFS analyses, the discrete nodules observed on *P. arundinacea* roots are composed of Mn and Zn carbonate phases.

Within anoxic and suboxic conditions, Mn(II) solubility is often limited by Mn carbonate phases (54, 55). Although, rhodochrosite may form a solid-solution series with smithsonite (ZnCO_3) (56), precipitation of smithsonite is kinetically limited under low temperatures and pressures; hydrozincite, on the other hand, is formed over a wide-range of $\text{CO}_{2(g)}$ partial pressures (57). Furthermore, if a solid-solution series was present on the plant roots, the chemical behavior of $\text{Mn}_x\text{Zn}_{(1-x)}\text{CO}_3$ would correspond more closely to ZnCO_3 rather than $\text{Zn}_5(\text{OH})_6(\text{CO}_3)_2$; yet, our data clearly supports

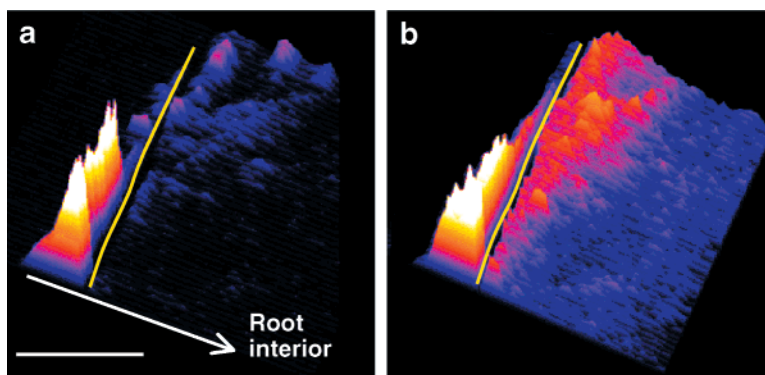


FIGURE 4. Two-dimensional X-ray microprobe image of (a) Mn and (b) Zn along a transect from the root center to the exterior of the plaque (scale bar represents 50 μm). Preserved roots were physically sliced in half longitudinally to reveal a cross-sectional view. The yellow line represents the root epidermis and relative elemental concentrations increase with color brightness.

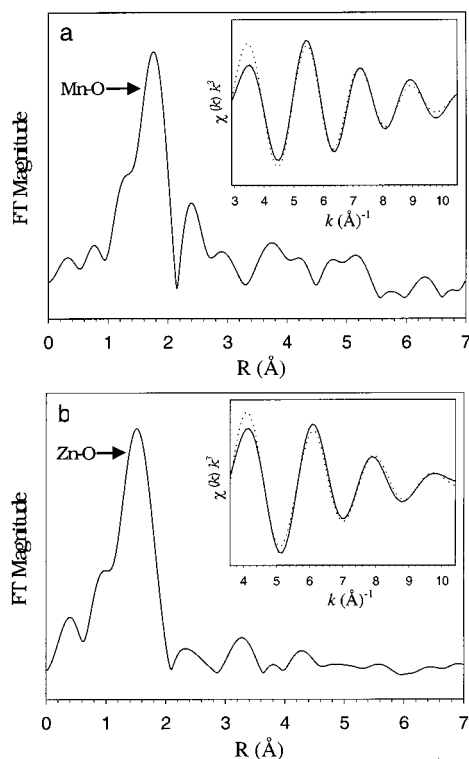


FIGURE 5. Fourier transformed (FT) spectra of (a) Mn and (b) Zn resulting in a radial structure function in real space (\AA). Fourier transforms are not phase-shift corrected and thus peak positions are less than true interatomic distances. Insets represent the k^3 weighted, backtransformed first shells [(a) Mn–O and (b) Zn–O] from the FT spectra illustrating the theoretical fits (dotted lines) to the experimental curve (solid lines).

formation of hydrozincite as the dominant phase of Zn. Structural dissimilarities among rhodochrosite and hydrozincite impedes epitaxial growth and subsequent solid-solution (57). As such, the nodules consist of multiple carbonate phases (mixed Mn/Zn carbonate, rhodochrosite, hydrozincite) in discrete domains within isolated nodules. Additionally, Ca is strongly correlated with Mn and Zn, and it is therefore likely that Ca carbonate (CaCO_3) is also associated with Mn and Zn deposition on root surfaces. Calcite may provide a substrate for initial Mn and Zn adsorption followed by either incorporation of the metals into the crystal lattice or rhodochrosite/hydrozincite precipitation. It has been noted that hydrozincite precipitates as discrete particles on calcite surfaces following an initial solid-solution reaction with Ca^{2+} in the surface layer (57, 58).

Accordingly, the precipitation and adsorption of Fe, Mn, Pb, and Zn at the root surface explains the high concentrations of metals associated with aquatic plant roots, and thus provides insight into the biogeochemical cycling of these metals within anaerobic systems. We have illustrated the complex sequestration mechanisms at the soil–root interface resulting from a substrate induced anoxic-oxic boundary (oxide precipitation), plant/bacterial respiration (carbonate nucleation), and microbial biofilm formation (metal complexation). Plant roots may thus provide a template for substantial metal sequestration in the form of adsorption complexes to either bacterial biofilms or iron (hydr)oxides or as mixed-metal carbonates.

Consequently, the retention of contaminants on the surface of plant roots is important in the cycling of nutrient and metal species. Considering that the mechanisms accounting for the metal-rich root rinds are common to most aquatic plants, this sequestration process may be appreciable within anaerobic soils, such as those within wetlands and rice paddies. Additionally, given that short-range-order hydrated iron oxides and organic functional groups have affinities for numerous metals (e.g., Pb, As), the Fe plaque-biofilm matrix will sequester many metals at the soil–root interface. Enhanced carbonate nucleation at the soil–root interface will also serve as a dominant control (as illustrated here) on divalent metals, such as Mn, Sr, and Zn. As such, predicting the fate and transport of metals within the rhizosphere is more complicated than predicted (not solely an Fe plaque influence), such that hydrated iron oxides, bacterial biofilms, and metal carbonates will influence the availability and mobility of contaminants within the sub-surface environment.

Acknowledgments

We gratefully acknowledge M. J. La Force and G. C. Li for help with sample collection and analysis. We also thank A. Templeton for use of the Pb EXAFS standard library and assistance with the Pb spectra linear combination fitting. This research was supported by the STAR Program of the U.S. EPA.

Supporting Information Available

Raman spectra of dehydrated plaque precipitate and analogous hematite standard. This material is available free of charge via the Internet at <http://pubs.acs.org>.

Literature Cited

- (1) Taylor, G. J. *J. Plant Nutr.* **1987**, *10*, 1213–1222.
- (2) Green, M. S.; Etherington, J. R. *J. Exp. Bot.* **1977**, *28*, 678–690.
- (3) Bartlett, R. J. *Soil Sci.* **1961**, *92*, 372–379.
- (4) Mendelssohn, I. A.; Postek, M. T. *Am. J. Bot.* **1982**, *69*, 904–912.

- (5) Davison, W.; Seed, G. *Geochim. Cosmochim. Acta* **1983**, *47*, 67–79.
- (6) Emerson, D.; Weiss, J. V.; Megonigal, J. P. *Appl. Environ. Microb.* **1999**, *65*, 2758–2761.
- (7) King, G. M.; Garey, M. A. *Appl. Environ. Microb.* **1999**, *65*, 4393–4398.
- (8) Crowder, A. A.; Macfie, S. M. *Can. J. Bot.* **1986**, *64*, 2120–2124.
- (9) St-Cyr, L.; Crowder, A. A. *J. Plant Nutr.* **1988**, *11*, 1253–1261.
- (10) Otte, M. L.; Rozema, J.; Koster, L.; Haarsma, M. S.; Broekman, R. A. *New Phytol.* **1989**, *111*, 309–317.
- (11) Taylor, G. J.; Crowder, A. A.; Rodden, R. *Am. J. Bot.* **1984**, *71*, 666–675.
- (12) Chen, C. C.; Dixon, J. B.; Turner, F. T. *Soil Sci. Soc. Am. J.* **1980**, *44*, 635–639.
- (13) Bacha, R. E.; Hossner, L. R. *Soil Sci. Soc. Am. J.* **1977**, *41*, 931–935.
- (14) Armstrong, W. Root aeration in the wetland condition. In *Plant Life in Anaerobic Environments*; Ann Arbor Science: MI, 1978; p 269.
- (15) Chen, C. C.; Dixon, J. B.; Turner, F. T. *Soil Sci. Soc. Am. J.* **1980**, *44*, 1113–1119.
- (16) Otte, M. L.; Dekkers, M. J.; Rozema, J.; Broekman, R. A. *Can. J. Bot.* **1991**, *69*, 2670–2677.
- (17) Wang, T.; Peverly, J. H. *Soil Sci. Soc. Am. J.* **1999**, *63*, 247–252.
- (18) St-Cyr, L.; Crowder, A. A. *Soil Sci.* **1990**, *149*, 191–198.
- (19) Bennett, E. H.; Siems, P. L.; Constantopoulos, J. T. In *Guidebook to the Geology of Northern and Western Idaho and Surrounding Area*; Idaho Geological Survey Bulletin 28; 1989; p 137.
- (20) Hobbs, S. W.; Griggs, A. B.; Wallace, R. E.; Campbell, A. B. *U.S. Geological Survey Professional Paper* **1965**, *478*, 1–28.
- (21) Javorka, E. In *Coeur d'Alene Basin Interagency Group, Coeur d'Alene Tribe of Idaho*; Coeur d'Alene Subagency: Plummer, ID, 1991; p 42.
- (22) La Force, M. J.; Fendorf, S. E.; Li, G. C.; Schneider, G. M.; Rosenzweig, R. F. *J. Environ. Qual.* **1998**, *27*, 318–328.
- (23) Galbraith, J. H.; Williams, R. E.; Siems, P. L. *Ground Water* **1972**, *10*, 33–44.
- (24) La Force, M. J.; Hansel, C. M.; Fendorf, S. E. *Environ. Sci. Technol.* **2000**, *34*, 3937–3943.
- (25) Hansel, C. M.; La Force, M. J.; Sutton, S. E.; Fendorf, S. In *Crerar Volume, Geochemical Society Special Publication*; Geochemical Society of America: 2001.
- (26) La Force, M. J.; Hansel, C. M.; Fendorf, S. E. *Soil Sci. Soc. Am. J.* **2000**, *64*, 809–811.
- (27) Hossner, L. R. Dissolution for total elemental analysis. In *Methods of Soil Analysis Part 3—Chemical Methods*; Soil Science Society of America: WI, 1996; p 56.
- (28) Klesta, E. J., Jr.; Bartz, J. K. Quality assurance and quality control. In *Methods of Soil Analysis. Part 3. Chemical Methods*; Soil Science Society of America: WI, 1996; pp 19–49.
- (29) Lytle, F. W.; Greigor, R. B.; Sandstone, D. R.; Marques, E. C.; Wong, J.; Spiro, C. L.; Huffman, G. P.; Huggins, F. E. *Nucl. Instrum. Methods Phys. Res. Sect. A* **1984**, *226*, 542–548.
- (30) Ressler, T. WinXAS 97; Hamburg, Germany, 1997.
- (31) George, G. N. EXAFSPAK; Stanford Synchrotron Radiation Laboratory, 1993.
- (32) Manning, B. A.; Fendorf, S. E.; Goldberg, S. *Environ. Sci. Technol.* **1998**, *32*, 2383–2388.
- (33) Schwertmann, U.; Cornell, R. M. *Iron Oxides in the Laboratory*; VCH: Weinheim City, Germany, 1991.
- (34) Schwertmann, U.; Fechter, H. *Clay Min.* **1994**, *29*, 87–92.
- (35) Ostergren, J. D.; Brown, G. E., Jr.; Parks, G. A.; Tingle, T. A. *Environ. Sci. Technol.* **1999**, *33*, 1627–1636.
- (36) Bargar, J. R.; Brown, G. E.; Parks, G. A. *Geochim. Cosmochim. Acta* **1997**, *61*, 2639–2652.
- (37) Manceau, A.; Charlet, L.; Boisset, M. C.; Didier, B.; Spadini, L. *Appl. Clay Sci.* **1992**, *7*, 201–223.
- (38) Porter, E. K.; Peterson, P. J. *Environ. Pollut.* **1977**, *14*, 255–265.
- (39) Lytle, C. M.; Smith, B. N. *Great Basin Natural.* **1995**, *55*, 164–168.
- (40) Johns, C. J. *Geochem. Explor.* **1995**, *52*, 193–203.
- (41) Hansel, C. M.; La Force, M. J.; Sutton, S.; Fendorf, S. E. *Environ. Sci. Technol.* Submitted for publication.
- (42) Eick, M. J.; Peak, J. E.; Brady, P. V.; Pesek, J. D. *Soil Sci.* **1999**, *164*, 28–39.
- (43) Xia, K.; Bleam, W.; Helmke, P. A. *Geochim. Cosmochim. Acta* **1997**, *61*, 2211–2221.
- (44) Templeton, A. S.; Ostergren, J. D.; Trainor, T. P.; Foster, A. L.; Traina, S. J.; Spormann, A.; Brown, G. E., Jr. *J. Synch. Rad.* **1999**, *6*, 642–644.
- (45) Manceau, A.; Boisset, M.; Sarret, G.; Hazemann, J.; Mench, M.; Cambier, P.; Prost, R. *Environ. Sci. Technol.* **1996**, *30*, 1540–1552.
- (46) Frenzel, P.; Bosse, U.; Janssen, P. H. *Soil Bio. Biochem.* **1991**, *31*, 421–430.
- (47) Gilbert, B.; Frenzel, P. *Soil Bio. Biochem.* **1998**, *30*, 1903–1916.
- (48) Perret, D.; Gaillard, J.; Dominik, J.; Atteia, O. *Environ. Sci. Technol.* **2000**, *34*, 3540–3546.
- (49) Friedl, G.; Wehrli, B.; Manceau, A. *Geochim. Cosmochim. Acta* **1997**, *61*, 275–290.
- (50) Effenberger, H.; Mereiter, K.; Zemanny, J. Z. *Kristallogr.* **1981**, *156*, 233–243.
- (51) O'Day, P. A.; Carroll, S. A.; Waychunas, G. A. *Environ. Sci. Technol.* **1998**, *32*, 943–955.
- (52) Ghose, S. *Acta Crystallogr.* **1964**, *17*, 1051.
- (53) Bedford, B. L.; Bouldin, D. R.; Beliveau, B. D. *J. Ecology* **1991**, *79*, 943–959.
- (54) Pedersen, T. F.; Price, N. B. *Geochim. Cosmochim. Acta* **1982**, *46*, 59–68.
- (55) Sternbeck, J. *Geochim. Cosmochim. Acta* **1997**, *61*, 785–793.
- (56) Böttcher, M. E. *Mineral. Magn.* **1995**, *59*, 481–488.
- (57) Zachara, J. M.; Kittrick, J. A.; Dake, L. S.; Harsh, J. B. *Geochim. Cosmochim. Acta* **1989**, *53*, 9–19.
- (58) Zachara, J. M.; Kittrick, J. A.; Harsh, J. B. *Geochim. Cosmochim. Acta* **1988**, *52*, 2281–2291.

Received for review January 18, 2001. Revised manuscript received July 9, 2001. Accepted July 11, 2001.

ES0105459